Materials & Design 215 (2022) 110443

Contents lists available at ScienceDirect

Materials & Design

journal homepage: www.elsevier.com/locate/matdes

BMP-2 incorporated biomimetic CaP coating functionalized 3D printed Ti6Al4V scaffold induces ectopic bone formation in a dog model

Yifei Gu [a], Lingfei Wei [b,e], Zheru Zhang [c], Jeroen Van Dessel [a], Ronald B. Driesen [d], Ivo Lambrichts [d], Reinhilde Jacobs [a], Lei Tian [c,*], Yi Sun [a,*], Yuelian Liu [b,*], Constantinus Politis [a]

[a] OMFS-IMPATH Research Group, Department of Biomedical Sciences, KU Leuven & Department of Oral and Maxillofacial Surgery, University Hospitals Leuven, Leuven 3000, Belgium
[b] Department of Oral Implantology and Prosthetic Dentistry, Academic Centre for Dentistry Amsterdam (ACTA), University of Amsterdam and Vrije Universiteit Amsterdam, Amsterdam, the Netherlands
[c] State Key Laboratory of Military Stomatology & National Clinical Research Center for Oral Diseases & Shaanxi Clinical Research Center for Oral Diseases, Department of Craniofacial Trauma and Orthognathic Surgery, School of Stomatology, FMMU, Xi'an, China
[d] Biomedical Research Institute, Hasselt University, Hasselt, Belgium
[e] Department of Oral Implantology, Yantai Stomatological Hospital, Yantai, China

HIGHLIGHTS

- A Ti6Al4V scaffold with optimal designing parameters and mechanical properties similar to cancellous bone was 3D-printed.
- To improve biocompatibility, a porous micro/nanostructured biomimetic calcium phosphate coating was applied to the scaffold.
- Using the coating as a carrier, bone morphogenic protein-2 was consistently and uniformly released in a cell-mediated manner.
- The bone morphogenic protein-2 integrated coating induced an even distribution of new bone formation within the scaffold.

GRAPHICAL ABSTRACT

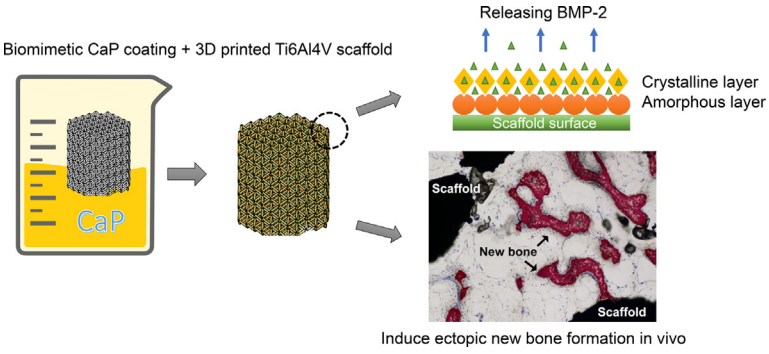

ARTICLE INFO

Article history:
Received 8 November 2021
Revised 13 December 2021
Accepted 29 January 2022
Available online 2 February 2022

Keywords:
Biomimetics
3D-printing
Titanium alloy
Bone morphogenetic protein 2
Calcium phosphate
Bone substitutes

ABSTRACT

The use of Ti6Al4V in bone engineering is limited, due to the biological inertia of the surface. In this study, a porous Ti6Al4V scaffold with mechanical properties similar to cancellous bone was designed and 3D-printed. Under physiological conditions, the scaffold was immersed firstly in a 5-fold-concentrated simulated body fluid, then in a supersaturated CaP solution containing BMP-2, to form a bone-like porous micro/nano structured biomimetic coating on the surface. Scaffolds were implanted in the muscle pouches created in six beagle dogs and were retrieved four weeks later for histologic and histomorphometric analysis. Results showed that BMP-2 integrated biomimetic CaP coating induced ectopic bone formation, which was absent in other two groups. Soft tissue infiltrated the scaffold's outside 1 mm layer, while the new-formed bone was evenly distributed in the longitudinal and horizontal directions within the rest of the scaffold based on BA/TA, BIC and BA measurements. In conclusion, the BMP-2 incorporated biomimetic CaP coating creates a micro/nano surface structure on the Ti6Al4V scaffold, which helps to increase biocompatibility. The integrated BMP-2 is capable of inducing ectopic bone formation in vivo.

* Corresponding authors.
E-mail addresses: tianleison@163.com (L. Tian), yi.sun@uzleuven.be (Y. Sun), y.liu@acta.nl (Y. Liu).

https://doi.org/10.1016/j.matdes.2022.110443
0264-1275/

The proposed combination may have the potential for bone reconstruction, but further studies are needed to explore its clinical applicability.

1. Introduction

The porous scaffold of different materials is one of the core elements in bone tissue engineering [1]. The interconnected pores in the scaffold provide channels for cell migration and the transportation of nutrition and oxygen. These pores also ensure the space for the formation of blood vessels and prevent necrosis of the new tissue due to insufficient vascularization [2].

Titanium and titanium alloys are widely used to manufacture scaffolds for their high strength-to-weight ratio, good biocompatibility, corrosion resistance and durability, strong osteointegration capability, and low cost [3,4]. However, disadvantages also exist: the elastic modulus of titanium and titanium alloy is 4–10 times than that of the human skeleton, and the mismatched mechanical properties between the material and the surrounding host bone are easy to cause the stress shielding effect; also, the low surface bio-recognition ability of titanium and titanium alloys has restricted their applications [5]. There is room for improvement in scaffold design, additive manufacturing (AM) technique, and surface modification.

In the medical field, 3D porous scaffolds have been produced through the AM technique (or 3D-printing technique) [6]. Interconnected porous constructs with predictable and predetermined unit cells were manufactured. The structure allows osteoblasts and mesenchymal stem cells to migrate and proliferate, as well as extramedullary tissues to infiltrate [7]. Moreover, the mechanical properties of the scaffolds can be modified by AM to approach those of human bone to relieve the stress-shielding effect [8].

Surface modification of metallic scaffolds improves the physical and chemical properties of the scaffold and enhances osseointegration [9]. Surface roughness at the micro/nano scale has been shown to aid in the bonding of bone and scaffold [10]. Calcium phosphate (CaP) is the most abundant mineral in bone minerals, and its degradation products provide abundant calcium and phosphorus to osteoblasts and promote bone regeneration [11]. Scaffolds coated with CaP show enhanced angiogenesis and bone formation based on its biocompatibility and osteoconductivity [12–14]. Bone morphogenic protein-2 (BMP-2) is one of the most potent growth factors that induce mesenchymal stem cell and osteoprogenitor cell differentiation into osteoblasts [15]. The BMP-2 integrated biomimetic CaP or CaP-based composites were fabricated under physiological temperature (37 °C) and pH conditions (7.4), and the biological activity of BMP-2 can be preserved during its coprecipitation with the inorganic components [16,17].

In previous studies, BMP-2 integrated biomimetic CaP coating with micro/nano structure was produced, and the excellent osteoinductive effects of this composited coating have been demonstrated in in vivo studies [16]. However, no research has ever attempted to combine the BMP-2 integrated biomimetic CaP coating with a 3D-printed porous titanium scaffold, which is designed in line with the biomechanical property of human bone. The advantages of the porous titanium scaffold mentioned above make it more conducive to repairing bone defects. More importantly, the 3D printed titanium scaffold can be customized for clinical applications and is more worthy of investigation.

The present study aimed to manufacture titanium alloy (Ti6Al4V) scaffolds via the AM technique. Biomimetic CaP coating (octacalcium phosphate, OCP) and BMP-2 were deposited on the scaffold surface simultaneously to promote the osteoconductive and osteoinductive properties of the scaffolds in an ectopic model in dog's back muscles. The objective is to see whether this combined fabrication is beneficial to new bone formation after four weeks of implantation.

2. Materials and methods

2.1. Design and 3D printing of the scaffold

Porous cylindrical models were designed in 3-Matic software (Materialise, Leuven, Belgium), and standard triangulation language (STL) files were created. The designed 3D model is shown in Fig. 1a. Porous cylinder Ti6Al4V scaffolds (diameter 10 mm, length 10 mm) were fabricated using a 3D Metal printer (ProX DMP 320, 3D Systems, Inc.) with a minimum feature size of 100 μm. Table 1 shows the scaffold designing parameters as well as the Ti6Al4V powder details. Ti6Al4V powder (LaserForm Ti Gr23 (A), 3D Systems, Inc.) was melted layer by layer in an argon atmosphere at a scanning speed of 1000 mm/s. According to previous numerical simulations [18,19], under this scanning speed, the instantaneous temperature within the molten pool during the selective laser melting of Ti6Al4V can reach approximately 3.5 ^ 10^3 K, with a heating rate of around 4.6 ^ 10^7 K/s and a temperature gradient of about 5.6 ^ 10^4 K/cm. A rapid solidification process was recorded (cooling rate of up to 5.5 ^ 10^5 K/s) after the laser beam left the Ti6Al4V molten pool. In total, 42 samples were printed, and 15 samples were randomly selected for the mechanical test, and the other 27 samples were randomly distributed to three groups (nine samples per group):

Group 1 (G1): Ti6Al4V scaffold without any coating (Ti6Al4V, Fig. 1b).
Group 2 (G2): Ti6Al4V scaffold with biomimetic CaP coating (CaP-Ti6Al4V, Fig. 1c).
Group 3 (G3): Ti6Al4V scaffold with BMP-2 incorporated biomimetic CaP coating (BMP-2/CaP-Ti6Al4V).

The distribution of scaffolds and the design of the experiment were shown in a flow chart (Fig. 2).

2.2. Procedures to perform coating

Samples in G2 and G3 were coated by biomimetic CaP using a well-established protocol (Fig. 1d) [20,21]. Briefly, the substrate coating of biomimetic CaP coating was deposited by immersing the Ti6Al4V scaffolds into 5-fold-concentrated simulated body fluid (5 L, 684 mM NaCl, 13.5 mM KCL, 9 mM $CaCl_2{\cdot}2H_2O$, 2.1 mM $Na_2HPO_4{\cdot}2H_2O$, 59.5 mM $NaHCO_3$, 5 mM $MgCl_2{\cdot}6H_2O$) for 24 h under physiological condition (37 °C, pH = 7.4). This treatment yielded a layer of amorphous CaP onto the scaffold surface. Then the scaffolds were sterilized using a standard steam autoclave procedure. Subsequently, the outside layer of biomimetic CaP coating was deposited onto the initial amorphous CaP substratum by immersing the scaffolds into supersaturated CaP solution (75 ml, 40 mM HCl, 137 mM NaCl, 4 mM $CaCl_2{\cdot}2H_2O$, 2 mM $Na_2HPO_4{\cdot}2H_2O$, 50 mM TRIS, PH: 7.4 ± 0.05) for 48 h under physiological condition (37 °C, pH = 7.4). This treatment yielded a layer of crystalline CaP onto the scaffold. In G3, recombinant human BMP-2 (rhBMP-2, Shanghai Rebone Biomaterials Co., China) was added into supersat-

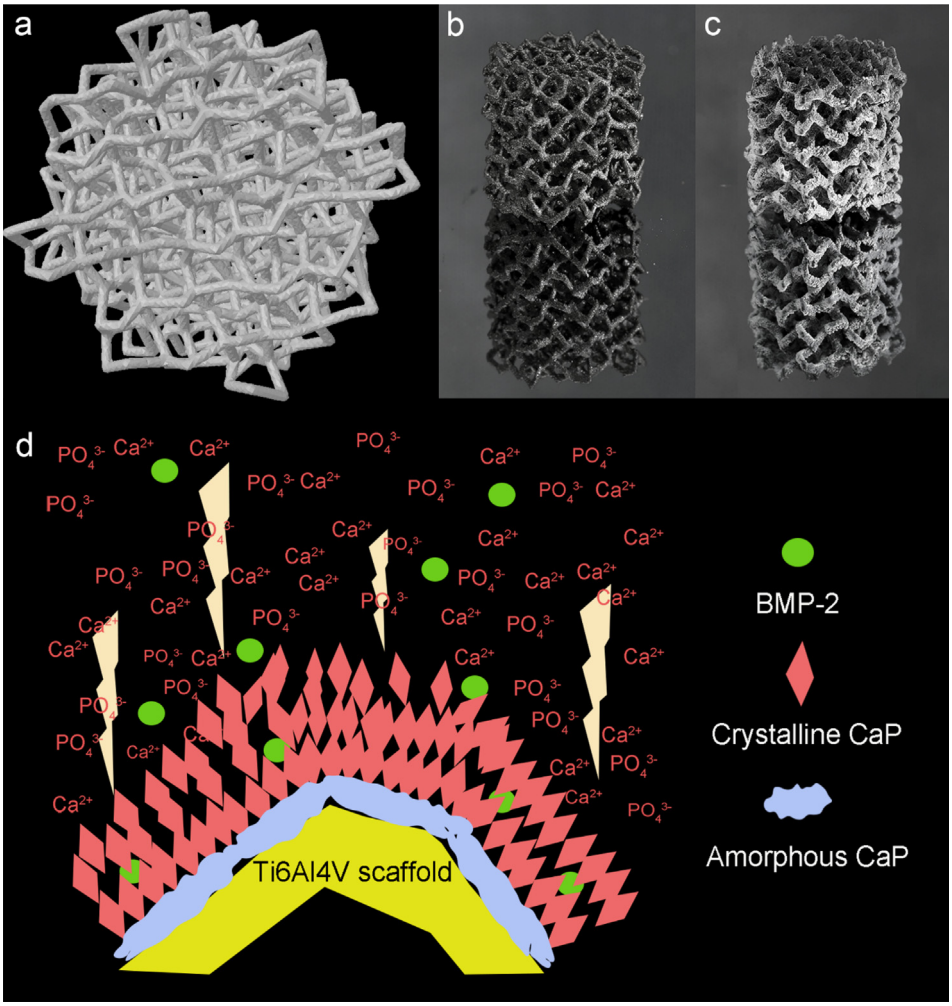

Fig. 1. Designed 3D model (a), uncoated Ti6Al4V scaffold (b) and Ti6Al4V scaffold with biomimetic CaP coating (c); (d) illustration of the fabrication process of biomimetic CaP coating. The lighting symbols in (d) indicate the direction of ion deposition.

Table 1
Designing parameters of the scaffold and information of the Ti6Al4V powder.

Designing parameters	Pore shape	Rhombic dodecahedron
	Pore size	438–825 μm (randomized distribution, average 638 μm)
	Porosity	88%
	Strut size	300 μm
Information of Ti6Al4V powder (manufacturer's data)	Composition (wt%)	Ti: Balance; N ≤ 0.03; Al: 5.5–6.5; C ≤ 0.08; V: 3.5–4.5; H ≤ 0.012; O ≤ 0.13; F ≤ 0.25; Y ≤ 0.005
	Particle size	100% < 1 mm

urated CaP solution at a concentration of 5 mg L^{-1} and was deposited simultaneously with the outside biomimetic CaP layer. The Ca/P ratio of the coating was determined by inductively coupled plasma-optical emission spectrometry (ICP-OES). The amount of BMP-2 incorporated into the coated scaffolds was determined by the ELISA technique [22]. Scaffolds were then dried and kept at room temperature. The entire procedure was performed under sterile conditions.

2.3. In vitro characterization

2.3.1. Mechanical test

The mechanical properties of the scaffold, including compressive strength and elastic modulus, were assessed by compression testing using a universal testing machine (Instron 4467, Instron Corp., USA) with a 5 kN load cell and a crosshead speed of 1 mm min^{-1} at room temperature. The ASTM E9-89a standard was followed for the compression test [23], and the tension-strain curves of the scaffold were recorded.

2.3.2. Micro-CT scan

Three scaffolds were randomly selected from each group (total n = 9, three in each group) and scanned with a micro-CT scanner (SkyScan 1172; Bruker-microCT, Kontich, Belgium) to calculate the porosity. The scanning parameters were set as: Pixel size = 1 0 × 10 μm; Step size = 0.25° per image; Filter = 1 mm thick Cu; Voltage = 100 kV; Current = 100 μA; Rotation = 360°. The scanning time for each step was approximately 1.6 s. The scanned images were then reconstructed with Bruker NRecon software (version 1.7.3.0) and the reconstructed axial images were analyzed by Bruker CTAn software (version 1.18.4.0). The porosity of the printed scaffolds was calculated within a selected region of interest (height: 3 mm, diameter: 8 mm, threshold: 128–255) in the middle of the scaffold.

2.3.3. SEM and EDX scan

After micro-CT scanning, the scaffolds (n = 3 in each group) were scanned with scanning electron microscopy (SEM) (Philips XL-30, FEI company, The Netherlands) to observe the surface mor-

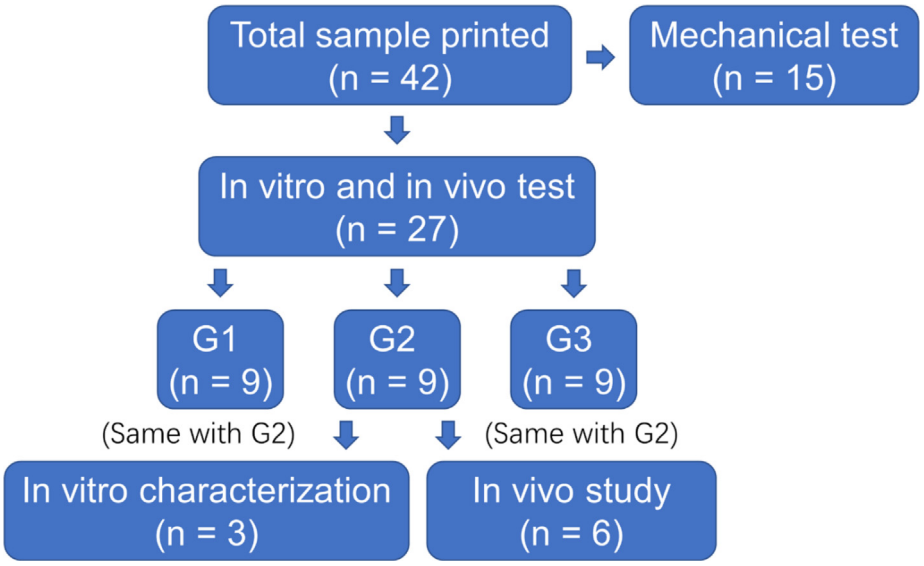

Fig. 2. The flow chart showing the distribution of scaffolds and the design of the experiment.

phology of the scaffold. Then, they were embedded with epoxy resin (Epofix resin, Struers, Copenhagen, Denmark) in cylindrical containers. The upper half (5 mm) of the scaffolds were removed by polishing and the middlemost cross-sections of the scaffolds were shown. The surface morphology of these cross-sections was characterized using SEM.

For each cross-section, a field of view was chosen at random, and three struts were chosen randomly within the field of view. The thicknesses of the struts were measured twice or three times in different locations, and the average strut thickness in each scaffold group was calculated. To observe the difference in coating thickness from the inside to the outside of the scaffold, three coated surfaces on the outer side of the scaffold and three coated surfaces in the center of the scaffold were randomly selected for each cross-section in G2 and G3, and the average coating thickness was measured and compared. The chemical composition of the biomimetic CaP coatings was characterized by an energy dispersive X-ray spectroscopy (EDX) attached to the SEM apparatus.

2.4. In vivo study

2.4.1. Study design

The research protocol was submitted to and approved by the Ethical Committee for Animal Experiments in The Fourth Military Medical University, China (No. 2018 (K9-023)). Six adult male beagle dogs with normal health status were selected and housed separately. The animals were provided with adequate diet and water, and the indoor environment was constant: temperature 18–19 °C; humidity 40–70%; routinely maintained air change 10–20 times per hour. Six scaffold samples from each group were used in the animal study.

After two weeks of adaptation and 12 h of fasting, the animals were fixed in prone position under general anesthesia (3% pentobarbital sodium solution 1 ml kg^{-1}, Intravenous injection). 8×10^6 Units of penicillin potassium were administered preoperatively. The backs of the animals were shaved and the skin was disinfected with iodophor and sealed with a hole towel. Incisions were firstly marked by methylene blue, then performed with a scalpel. The connective tissues were fully separated until the erector spinae showed. Three muscle pouches were made by separating the muscle fibers along the spine, and an about 3 mm distance was kept between every muscle pouch and the spine to prevent potential nerve injuries. For each animal, one scaffold from each group was randomly selected and implanted into the three muscle pouches. After implantation, the muscle pouches, perimysium, subcutaneous tissues and skin were closed with suture in order, and the wound was cleaned with 75% ethanol and dressed tightly. The animals were given five days of anti-inflammatory drugs after surgery. At week 4 after implantation, the animals were anesthetized and fixed with the same method described above. The muscle pouches were opened again, and the scaffolds were harvested and kept in 10% formaldehyde solution, followed by storing in 4 °C refrigerator. The processes of suturing, disinfecting and dressing were the same as described above, and the animals were observed and taken care of properly. The dressing was removed three days after the surgery.

2.4.2. Histological and histomorphometrical analysis

Retrieved scaffolds were rinsed with ultrapure water at room temperature for 24 h and dehydrated by graded ethanol (70%–100%) for 48 h. The samples were then vitrified with dimethylbenzene and embedded with polymethyl methacrylate (PMMA). Five sections of 200 μm in thickness were vertically cut from the scaffold (Fig. 3a). The cut sections were polished into 30–50 μm thick sections with sandpapers, and then stained with McNeil's Tetrachrome, basic Fuchsine and Toluidine Blue O. The images of each slice were obtained using a light microscope (Axio-Imager M2, Carl Zeiss Microscopy, Jena, Germany) to observe new bone induction.

On each section, the most top, bottom, left and right points of the scaffold were marked using Image J software, and the center of the section was determined by crossing the top–bottom line and the left–right line. Five concentric circles, centered at the center of the scaffold and with diameters of 1 to 5 mm, were drawn and called circle 1 to circle 5 respectively (Fig. 3b). Based on these circles, five regions of interest (ROI) were set: ROI1 = range of circle 1; ROI2 = ring-shaped area of circle 2 minus circle 1; ROI3 = ring-shaped area of circle 3 minus circle 2; ROI4 = ring-shaped area of circle 4 minus circle 3; ROI5 = ring-shaped area of circle 5 minus circle 4.

To observe the distribution of the new bone, the following tests were performed in horizontal and longitudinal directions:

In the horizontal direction, in each ROI, the parameters of observed new bone around the scaffold, including tissue area (TA, mm^2), bone area (BA, mm^2) and bone to implant contact

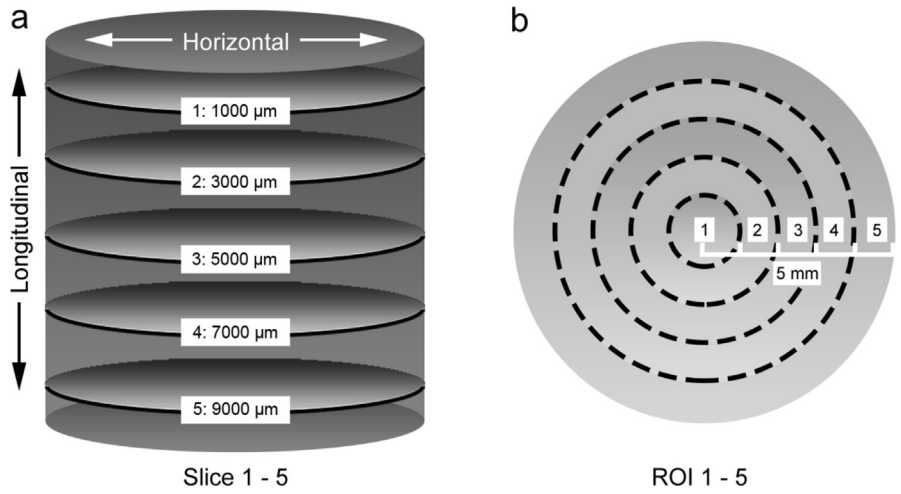

Fig. 3. Schematic diagram for slice 1–5 and ROI 1–5 in each scaffold. Slice 1–5 and ROI 1–5 were used to assess the longitudinal and horizontal distribution of new bone, respectively.

(BIC, %) were quantitatively evaluated using Image J software. The bone area fraction was calculated by BA/TA. The BA/TA and BIC values were compared between different ROI groups.

In the longitudinal direction, BA, BA/TA and BIC values were calculated and compared between different slice groups to evaluate the longitudinal distribution of new bone.

In the end, five regions with new bone were randomly selected in the slice 2 and slice 4 of every scaffold, respectively. The area of bone (mm^2), as well as the number of cells in the new bone (osteocytes, osteoblasts and osteoclasts) were measured and counted using Image J software, and the cell density was calculated by cell number/bone area.

2.5. Statistical analysis

The data obtained from the in vitro characterization and animal study were analyzed and expressed as mean ± deviations. The statistically significant difference (p-value) was calculated using the SPSS statistics software (SPSS 26.0). Statistical method was selected based on whether the calculated data follows a normal distribution. A p-value lower than 0.05 was considered to be significant.

3. Results

3.1. In vitro characterization

The scaffolds were successfully printed and coated, and the samples remained intact without any fractures throughout the entire experimental process. The amorphous layer had a Ca/P ratio of 1.78, while the crystalline layer had a Ca/P ratio of 1.63. The loading of BMP-2 (266 ± 41 μg per scaffold) was further confirmed by ELISA technique.

3.1.1. Mechanical test

With respect to the mechanical properties of Ti6Al4V and CaP, it is unlikely that the mechanical properties of the scaffold will be changed due to the addition of biomimetic CaP coating. The mechanical test revealed that the compressive strength and elastic modulus of the tested Ti6Al4V scaffolds were 17.4 ± 0.7 MPa and 1.64 ± 0.12 GPa, respectively.

3.1.2. Micro-CT scan

The total porosity of the scaffolds in the three groups was determined by micro-CT: G1, 84.8%; G2, 83.8%; G3, 83.8%. The presence of the biomimetic CaP coating slightly reduced the total porosity of the scaffold. Moreover, the actual porosity of the Ti6Al4V scaffold was lower than that of the designed porosity (88%) because of the existence of unmelt pools formed during sintering.

3.1.3. SEM and EDX scan

Figs. 4–6 show the SEM images of the surface and cross-sectional characteristics of three groups of scaffolds, respectively. SEM pictures demonstrate the rough metal surface induced by the sintering of alloy powder particles (Fig. 4b) and the coated scaffold surface completely covered with micro/nanostructures (Fig. 4d and f). The high magnified SEM image contrasts the rough surface of the titanium scaffold with the crystallized coating surface, which is composed of vertically stacked plate-like nano-thick crystallites (Fig. 5). On cross-sections, a clear boundary can be observed between the base layer of the amorphous CaP and the outer layer of the crystalline CaP (the yellow dotted line in Fig. 6). In addition, clear boundaries can also be observed between the whole CaP coating, the scaffold and the epoxy resin under the backscattered electron mode (Fig. 6e and f). According to the previous research [24], the amorphous layer is a dense and homogenous CaP film made up of spherical CaP pellets with a diameter of about 100 nm that serves as seeds for the crystalline layer's secondary nucleation. Previous studies have also proved that the crystallites possess the features typical of an OCP crystal structure through the X-ray diffraction and the Fourier transform infrared spectroscopy examinations [20,21], irrespective of the absence or presence of BMP-2 [20]. Moreover, the form of the coating was not affected by the incorporation of BMP-2.

Results of strut thickness and coating thickness measurement are shown in Fig. 7. The mean strut thicknesses of scaffolds in G2 (316.8 ± 19.1 μm) and G3 (322.31 ± 12.9 μm) were shown to be significantly higher than that of the scaffolds in G1 (293.17 ± 27.2 μm, $p < 0.05$). No significant difference was observed in the mean strut thickness between G2 and G3. The average coating thickness was significantly higher on the outer part of the scaffold than in the center of the scaffold in G2 (17.20 ± 2.03 μm vs. 7.12 ± 1.24 μm, $p < 0.05$), and the same result was observed in G3 (17.52 ± 2.35 μm vs. 6.76 ± 0.84 μm, $p < 0.05$). No significant difference was observed in the mean coating thickness between G2 and G3. EDX results confirmed that chemical elements including C, O, Na, Mg,

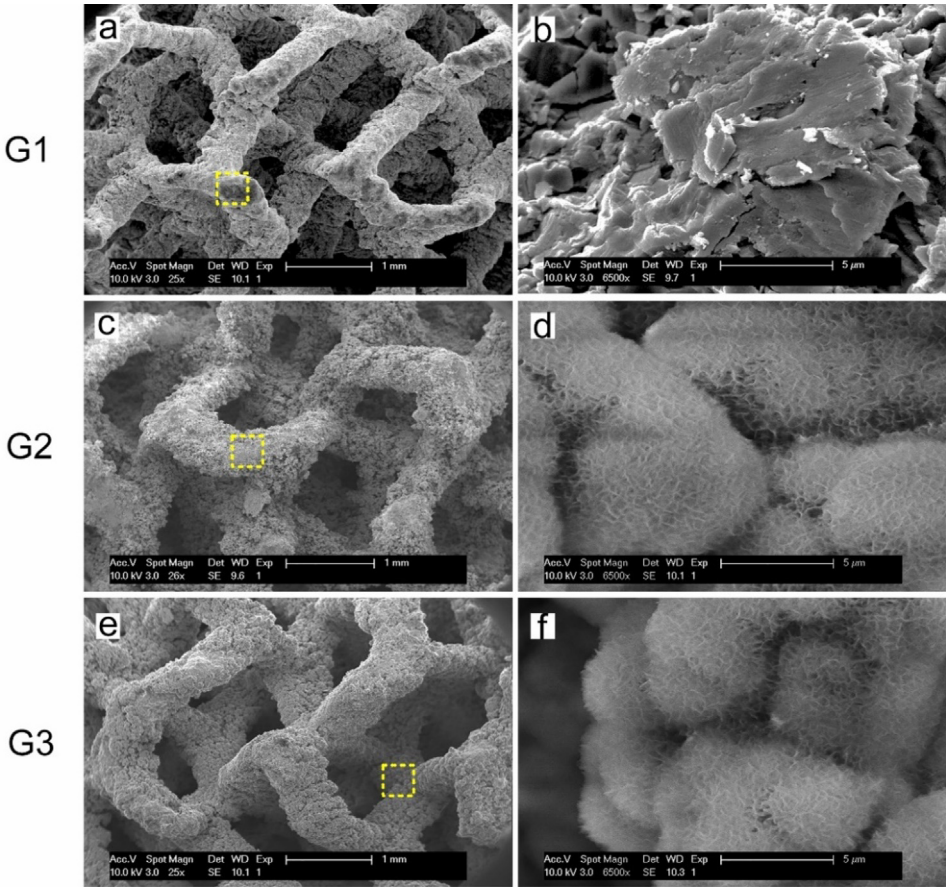

Fig. 4. SEM images of the surface characteristics of scaffold in G1 (a and b), G2 (c and d) and G3 (e and f). The images in the right column are the magnified images of the yellow boxes in the left column.

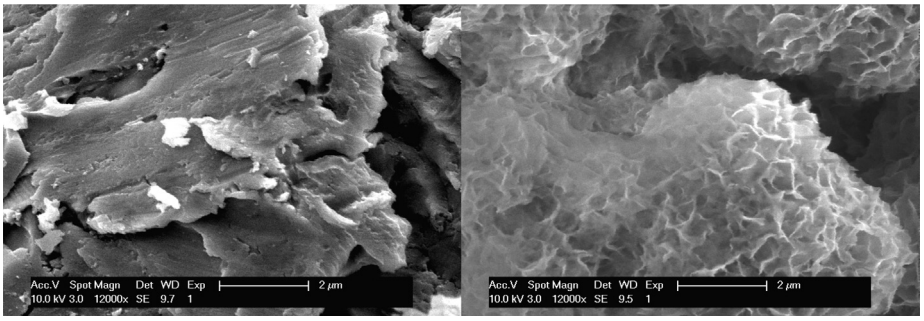

Fig. 5. SEM images contrasting the coarse scaffold surface with the coating surface, which is made up of nano-thick plate-like crystals.

Si, P, Cl and Ca could be observed in the biomimetic CaP coating. There was no apparent change in the elemental composition of the coatings between G2 and G3 (Appendix A). Mg^{2+} is used to inhibit crystal growth and promote the formation of an amorphous CaP layer, and it only exists in the amorphous layer, not the crystalline layer [16].

3.2. In vivo characterization

All animals remained alive by the end of the study. The wounds of two animals were not healed one week after the surgery and the scaffolds were rejected from the surgical site due to the inflammatory reactions. Consequently, these two animals were excluded from the subsequent study. The experimental sites in the remaining four animals healed uneventfully without significant complications. In total, there are four valid samples for our analysis in each group.

3.2.1. Histologic observation

Fig. 8 showed that in G1 and G2, only loose connective tissues were observed in the scaffold. Bone induction is seen only in the BMP-2 integrated biomimetic CaP coating (G3, Fig. 8c). The formed trabeculae were separated from the muscle tissue by a layer of infiltrated soft tissue (Fig. 8f).

Fig. 9 showed the details of the new bone in G3. The new bone was either attached to the scaffold surface, or grew free in the space between the scaffold struts, and the bone islands were interconnected to form a trabecular network. Around the trabeculae is the loose connective tissue full of new-forming blood vessels (Fig. 9a). Direct bone to implant contact can be found (Fig. 9b

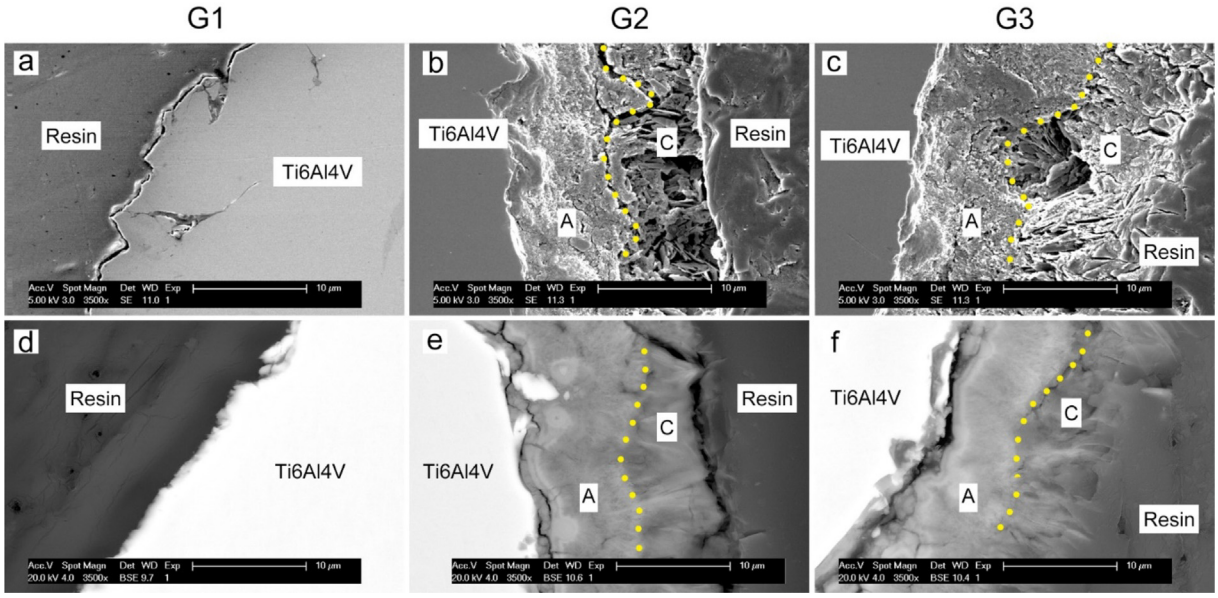

Fig. 6. SEM images of the cross-sectional characteristics of scaffold in G1, G2 and G3. (a) to (c) are pictures viewed in the secondary electron mode, and (d) to (f) are pictures viewed in the backscattered electron mode. The yellow dotted line represents the boundary between the amorphous CaP coating (A) and the crystalline CaP coating (C).

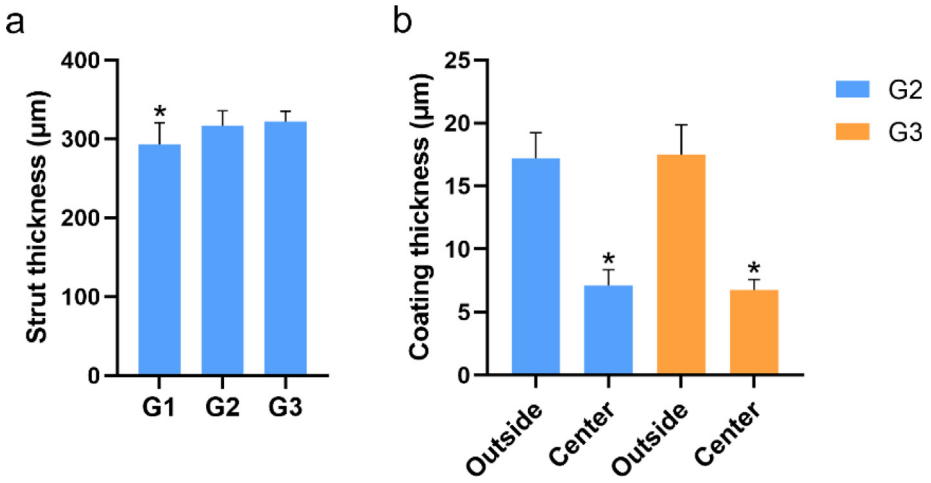

Fig. 7. Measurement results of strut thickness and coating thickness. * in (a) means the strut thickness of scaffolds in G2 and G3 was significantly different from that in G1; * in (b) means the coating thickness in the center of the scaffold was significantly different to that on the outside part of the scaffold in G2 and G3.

and c). The new-formed bone was normal in appearance, and the mineralized bone matrix, osteoblasts, osteoclasts, and osteocytes were visible (Fig. 9d).

3.2.2. Histomorphometrical analysis

Histomorphometrical analysis was only performed in G3 (sample n = 4, slice n = 20) since no new-formed bone was observed in other two groups. The cell density in the new bone was 1274 ± 307 / mm^2. Results of BA/TA, BIC and BA measurements are shown in Fig. 10.

In the horizontal direction of the scaffold, ROI5 was mostly filled with muscle fibers and soft tissues grown from the surrounding muscle tissues, so new bone formation has hardly been observed in ROI5. Normal distribution detection revealed that, except for ROI5, the BA/TA and BIC values of the other four ROI groups were consistent with normal distribution characteristics. The Kruskal-Wallis H test results showed that the distributions of BA / TA and BIC values between ROI1 to 5 groups were not all the same, and the differences were statistically significant ($p < 0.05$). The post-hoc pairwise comparison revealed that the distribution of BA / TA and BIC values in ROI5 were significantly different from that in each of the other four ROI groups ($p < 0.05$), between which there was no significant difference ($p > 0.05$). To improve the analytical precision, the ANOVA test was further applied between ROI1 to 4 groups, and no significant differences in mean BA/TA ($F = 2.71$, $p = 0.05$) and BIC ($F = 2.51$, $p = 0.06$) values were found between these four groups. The results revealed that the new bone expanded uniformly within a range of 4 mm from the center of the scaffold, and the soft tissue could only penetrate around 1 mm into the scaffold.

In the longitudinal direction of the scaffold, The BA/TA and BA values in slices 1 to 5 groups all followed a normal distribution, but not all of the BIC values did. ANOVA test showed no significant difference in the mean BA/TA ($F = 0.72$, $p = 0.58$) and BA ($F = 0.89$, $p = 0.49$) values between slice 1 to 5 groups. Kruskal-Wallis H test showed that no significant difference was found in the distribution of BIC values between slice 1 to 5 groups ($p = 0.81$). These results indicate that the new bone develops uniformly along the scaffold's long axis.

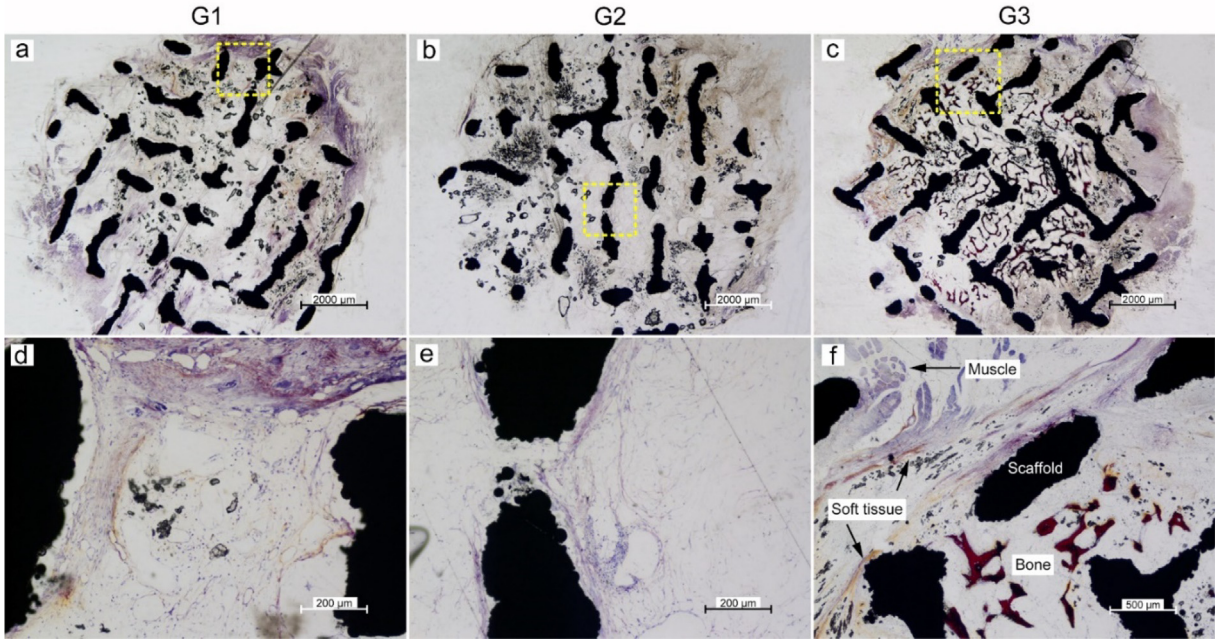

Fig. 8. Histological images of scaffold in G1 (a and d), G2 (b and e) and G3 (c and f). The images in the bottom row are the magnified images of the yellow boxes in the top row. (f) indicates that the infiltrated soft tissue functions as a boundary between the muscle tissue and the new bone.

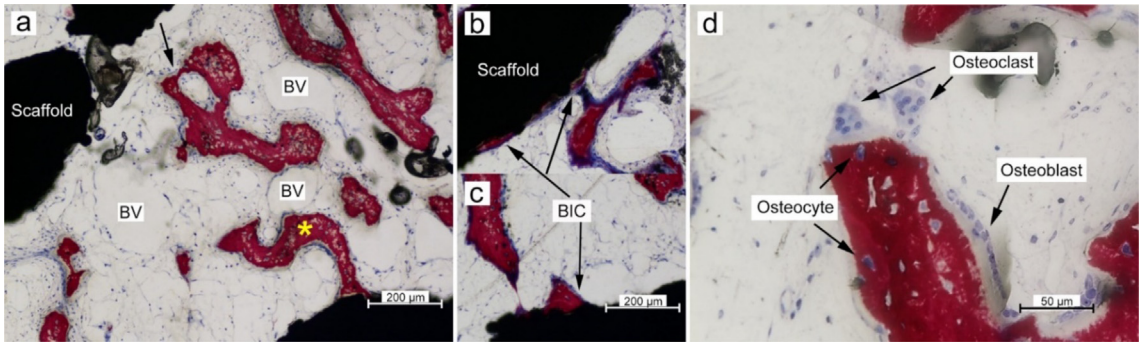

Fig. 9. Details of the new bone in the histological images of scaffold in G3. (a) shows the free bone islands and those attached to the scaffold surface (marked by *), and the interconnected trabecular network (arrows). The surrounding loose connective tissue is full of forming blood vessels (BV). (b and c) show the direct bone to implant contact (BIC) between new bone and the scaffold. (d) shows the new bone with osteocytes, and the aligned osteoblasts and osteoclasts.

4. Discussion

At present, research on AM scaffold focuses primarily on mechanical properties in vitro. Factors, including design parameters, printing techniques and selection of coatings, are closely linked to the biological characteristics of the scaffold, which can be most effectively verified by in vivo studies.

Our research is the first study combining BMP-2 incorporated biomimetic CaP coating with porous Ti6Al4V scaffold, and our result has shown that this combination promotes ectopic bone formation. One of the findings in our study is that the addition of BMP-2 determines the ectopic bone formation, and the new bone tissue was observed only in G3. Only loose connective tissue was observed around the scaffold struts in G1 and G2, meaning that the biomimetic CaP coating alone was unable to stimulate bone regeneration in the muscle pouches made in beagle dogs. Another interesting finding is that in G3, although the coating thickness on the center and the outside of the scaffold was not uniform, the BA/TA, BIC and BA values were not significantly different between five slice groups in the longitudinal direction. Besides, in the horizontal direction, there were no significant differences in BA/TA and BIC values between five ROI groups. This implies that the apparent new trabeculae in the scaffold were evenly distributed both longitudinally and horizontally. We assumed that the infiltrated soft tissue 'wrapped' the released BMP-2 and allowed it to spread in limited space within the scaffold, resulting in the new trabeculae spreading evenly throughout the scaffold.

BMP-2 belongs to the transforming growth factor-beta family and induces ectopic bone formation [25]. BMP-2 integrated biomimetic CaP composites have been prepared and coated to various materials (including Ti6Al4V) in previous in vitro and in vivo studies. The coated composite preserves the biological activity of the rat bone marrow stromal cells while also increasing their ALP activity [17]; and in another study, increases the proliferation and promote the osteogenic differentiation of MC3T3-E1 cells [26]. In addition, the long-term sustainable osteogenic differentiation capacity of the BMP-2 coating has been demonstrated at both ectopic [27–29] and orthotopic [30] sites in vivo. In addition, the long-term sustainable osteogenic differentiation capacity of the BMP-2 coating has been demonstrated at both ectopic [27–29] and orthotopic [30] sites in vivo. However, a previous study revealed that a single, rapid uptake of high dose BMP-2 stimulated resorption of newly formed bone [28]. Therefore, ensuring a long-term effect of BMP-2 on osteogenic differentiation and limiting

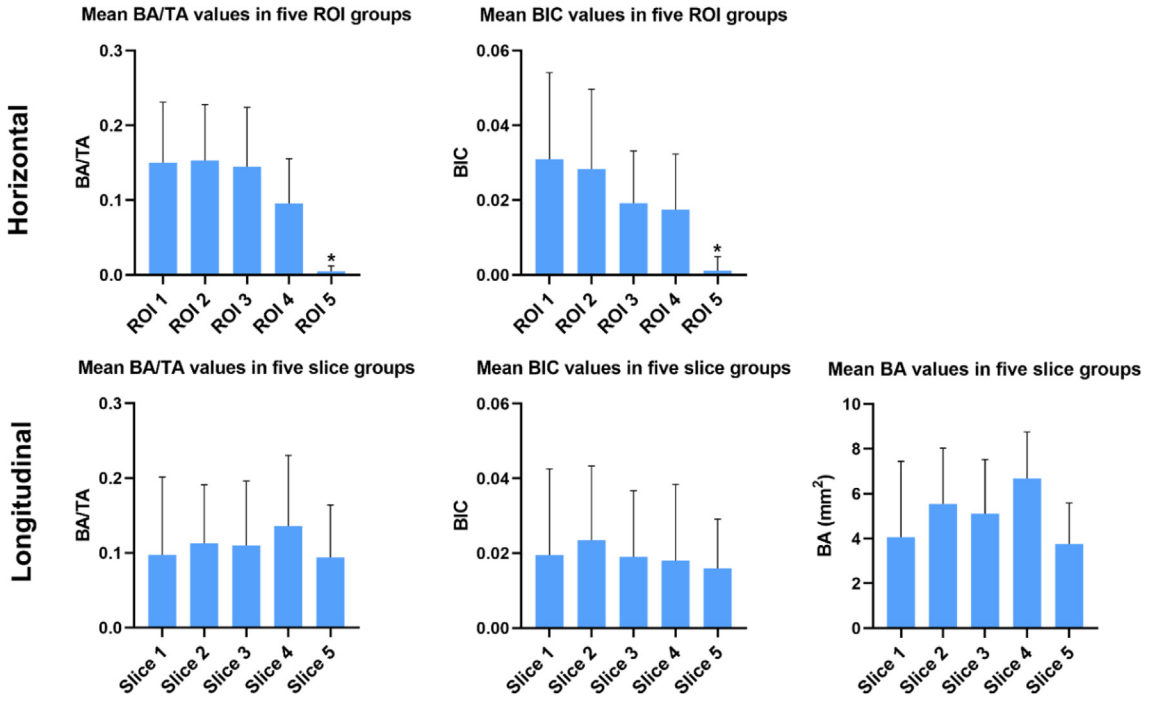

Fig. 10. BA/TA, BIC and BA measurements in five ROI groups and five slice groups. *means the BA/TA value in ROI 5 group was significantly different from that in ROI 1 to 4 groups in BA/TA and BIC measurements.

extensive bone resorption requires a drug loading system (carrier) which permits a steady and sustained release of BMP-2.

Biomimetic CaP coating was used as a carrier of BMP-2 in this study. The micro/nano hybrid structure has been shown in studies to improve osteoblast adhesion, proliferation, and differentiation. Moreover, the micro/nano structure can provide a larger specific surface area, which can improve protein anchoring and adsorption effectiveness and ability [31]. The first precipitated amorphous CaP particles in the biomimetic coating act as nucleation sites for the subsequent crystal growth, and OCP crystals grow epitaxially on the surface of this seeding layer [32]. The morphology of the amorphous CaP particles changes when they come into contact with the supersaturated CaP solution, which was manifested as an increase in particle size and partial dissolution, which then initiates the nucleation and growth of OCP crystals perpendicular to the seeding layer [33].

It is hypothesized that the BMP-2 was liberated from the inorganic matrix based on the synergistic resorptive activities of the foreign body giant cells and the osteoclasts [20]. Moreover, this cell-mediated release process for BMP-2 is supposed to be similar to the physiological bone remodeling process by virtue of growth factors being released from the bone matrix during its degradation [16,17]. In addition, the surmise is supported by previous studies showing that the bone induction performance of the coating-incorporated BMP-2 depot was markedly higher than the utilization of a surface-absorbed BMP-2 depot [20,34].

BMP-2 is released in a slow MC3T3-E1 and sustained mode since the distribution density of BMP-2 is fixed in the supersaturated CaP solution [17,34,35]. The release mechanism of coating-incorporated BMP-2 was determined in vivo previously by using a radiolabeled osteogenic agent (^{131}I-BMP-2) [36]. Results showed that 50% of the BMP-2 loaded was released over five weeks (5% to 10% weekly), and a stable and effective osteogenic response was obtained with a low pharmacological dose of BMP-2. Apart from being a carrier, the integration of BMP-2 also strengthens the CaP coating by surrounding the brittle CaP crystals and enhances the coating's binding to the underlying titanium alloy substrate [37]. This kind of mutual benefit grants biomimetic CaP coating a distinct advantage over other BMP-2 carriers in bone reconstruction. However, in the current study, we must admit that the low concentration ratio of BMP-2 to CaP makes it difficult to judge the strengthening effect of BMP-2. To maximize coating strength and biocompatibility, further research is required to optimize the amount of protein integrated into the coating.

We hypothesize that BMP-2 was slowly released from the progressively degraded CaP coating in a cell-mediated manner and induced an even distribution of new bone formation within the scaffold. Osteoblasts and osteoclasts around the trabeculae help to expand and reshape the trabeculae into the cancellous bone. New blood vessels around the trabeculae carry the bone progenitor cells, nutrients, and oxygen. New bone trabeculae were formed through a direct ossification mechanism instead of the enchondral mechanism, which was also identified in some previous in vivo studies [20]. Direct ossification occurs in a mechanically stable environment provided by the porous scaffold [20]. The surface of the scaffold had a thicker biomimetic CaP coating and a higher amount of integrated-in BMP-2. However, we observed that the 1 mm-thick outer rim of our scaffolds was occupied by only soft tissue. The absence of direct ossification could be explained by continuous exposure of the outer rim to a mechanically unstable environment. The latter would be induced via the frictional contact between the scaffold surface and the beagle dog's back muscles during movement.

In this study, the Ti6Al4V scaffold was designed to meet the optimal pore size (100 to 1200 μm) [38] and porosity (80% to 90%) [39] for cell proliferation and migration, as well as the smooth delivery of oxygen and nutrients. In addition, the scaffold mimicked the cancellous bone's mechanical characteristics, that is, an elastic modulus of 0.2–2 GPa and compressive strength value of 2–80 MPa [40]. The porous system's mechanical properties can be easily controlled by changing the porous structure, and the balance between these two aspects must be maintained. Apart from pore size and porosity, the pore unit's shape also significantly impacts the scaffold's biological and mechanical properties. How-

ever, it should be noted that, since porosity and pore size may also change along with variations in the pore unit, it is difficult to determine which pore unit is most conducive to new bone formation. Few articles have explicitly examined the pore unit's impact on the scaffold's osteogenesis capability. With a view to optimizing pore size and porosity, we selected the rhombic dodecahedron unit, which has been extensively researched in the designing and manufacturing of porous bone scaffold [41–43], in our experiment. Several other studies have also developed 3D printed porous Ti6Al4V scaffolds with mechanical characteristics similar to cancellous bone, with porosity varying from 22% to 80% [44–47]. A balance has been established between high porosity and appropriate mechanical property in our designed scaffold compared to their findings.

Despite our major advancement in ectopic bone formation, our study presents some limitations. Considering the scaffold's limited permeability, the supersaturated CaP solution could not fully penetrate every part of the scaffold. As a result, the coating thickness in the middle of the scaffold was lower than that at the scaffold's surface. The limitation of permeability was partly due to the porous structure's design and, on the other hand, to the fact that a large number of titanium alloy powders were only partially remelted during the AM manufacturing process, resulting in high surface roughness of the scaffold [48]. According to our hypothesis, the infiltrated soft tissue 'wrapped' BMP-2 and allowed for good ectopic bone formation in this study. However, ensuring a uniform thickness of the coating would improve the overall osteogenic differentiation capacity of the scaffold in an open environment. Currently, the AM procedure inevitably creates defects such as irregular pore shapes or micro-pores within the AM components and thus requires further research in optimizing the AM parameter management and processing technique. A second limitation relates to the infiltration of soft connective tissue which hinders bone formation. The limited bone formation would not be conductive to the fixation of the porous scaffold if the scaffold has been applied to repair the bone defect. To prevent rapid ingrowth of soft tissue within the pores, the use of a collagen membrane should be considered to separate the scaffold's surface from the soft tissue.

Some critical challenges still remain in the phase of biomaterial development and scaffold design. First, more and more new biomaterials, such as Ti-7.5Mo alloy, have been explored with AM technology's advancement. Ti-7.5Mo alloy has been shown to have a lower elastic modulus and more potent strength/modulus combination than titanium and titanium alloy; it is also known to be a material of excellent corrosion resistance and biocompatibility [49]. Several previous studies have successfully developed Ti-7.5Mo alloy scaffolds, which comply with cancellous bone's mechanical requirements [49–51]. Using in vivo experiments to confirm this scaffold's biocompatibility is also our aim in the next step. Secondly, the perfect bone tissue scaffold material should be biodegradable, leaving only healthy bone tissue within the human body. Thirdly, as for the scaffold design, there is still a lack of a unified standard. The optimized option of pore unit, for example, has not yet been determined. Future studies should concentrate on a general understanding of how the scaffold's geometric parameters impact the scaffold's mechanical and biological behavior. In the fourth place, the natural bone consists of four different levels of pore sizes, and the composition of the bone continually varies according to its stress state [52]. Functional grading scaffolds can mimic the shape and structure of natural bones and encourage tissue growth while maintaining mechanical strength [53]. Functionally grading scaffolding has also been widely studied in recent years, in which porosity varies within the scaffold with a particular gradient [54–56]. This structure can also be considered to repair long bone defects, which is also a key element in future research. Finally, the sterilization of BMP-2 coated implants is an important issue that has not been adequately addressed. Guillot et al. found that the osteoinductive potential of BMP-2 coated on titanium implant was retained following sterilization with the method of 25 kGy gamma radiation, and the amount of BMP-2 remaining after irradiation was still sufficient to induce new bone tissue [57]. Furthermore, 25 kGy gamma radiation sterilization has been used to sterilize biological materials containing BMP-2 in other studies [58–61]. This potential sterilization method may be applied to the future industrial production of the scaffold, but more research is required to verify its clinical safety and effectiveness.

5. Conclusion

In conclusion, we have manufactured a porous Ti6Al4V scaffold with similar mechanical properties to the cancellous bone in a beagle dog model. Using biomimetic CaP coating as a carrier, BMP-2 was attached to the scaffold's surface to promote ectopic bone formation. BMP-2 incorporated biomimetic CaP coating greatly improved new bone formation in vivo. The proposed coating of a 3D-printed porous scaffold seems to offer some future potential for bone tissue reconstruction, with more studies needed to assess its clinical feasibility.

6. Ethical statement*a

The research protocol was submitted to and approved by the Ethical Committee for Animal Experiments in The Fourth Military Medical University, China (No. 2018 (K9-023)).

7. Data availability statement*a

Data regarding this article is available from the corresponding author upon a reasonable request.

CRediT authorship contribution statement

Yifei Gu: Methodology, Investigation, Data curation, Writing – original draft. **Lingfei Wei:** Methodology, Formal analysis, Writing – review & editing. **Zheru Zhang:** Investigation, Resources. **Jeroen Van Dessel:** Investigation, Formal analysis. **Ronald B. Driesen:** Formal analysis, Writing – review & editing. **Ivo Lambrichts:** Formal analysis, Resources. **Reinhilde Jacobs:** Resources, Writing – review & editing. **Lei Tian:** Conceptualization, Supervision, Funding acquisition. **Yi Sun:** Conceptualization, Supervision, Project administration. **Yuelian Liu:** Conceptualization, Supervision, Project administration. **Constantinus Politis:** Supervision, Resources, Project administration.

Declaration of Competing Interest

The authors declare that they have no known competing financial interests or personal relationships that could have appeared to influence the work reported in this paper.

Acknowledgements

We acknowledged the contributions of all members of our research group to this article. This research was granted by National Natural Science Foundation of China(NSFC) No. 81670964, and Shandong Taishan Scholar Program to Dr. Yuelian Liu. The authors appreciate Shanghai Rebone Biomaterials Co. for the supply of BMP-2.

Appendix A

A.1. EDS result of scaffold in G2

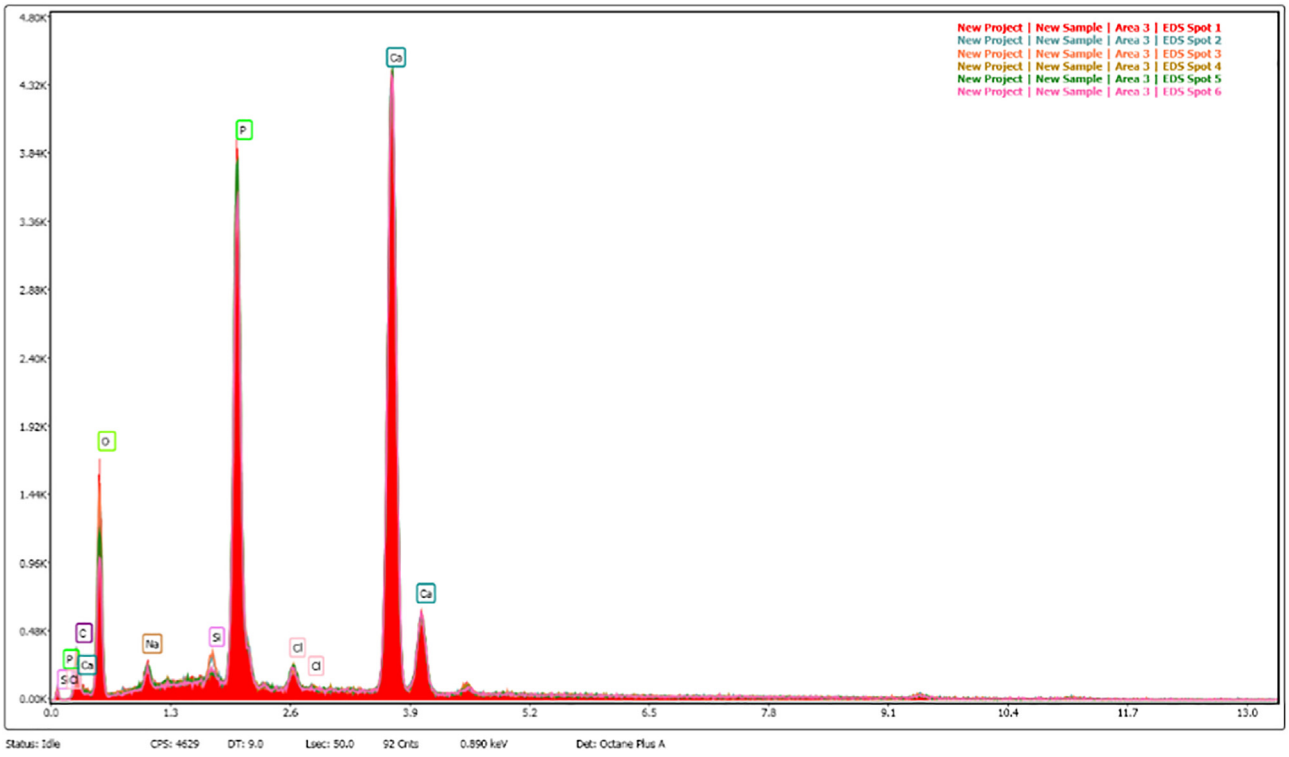

A.2. EDS result of scaffold in G3

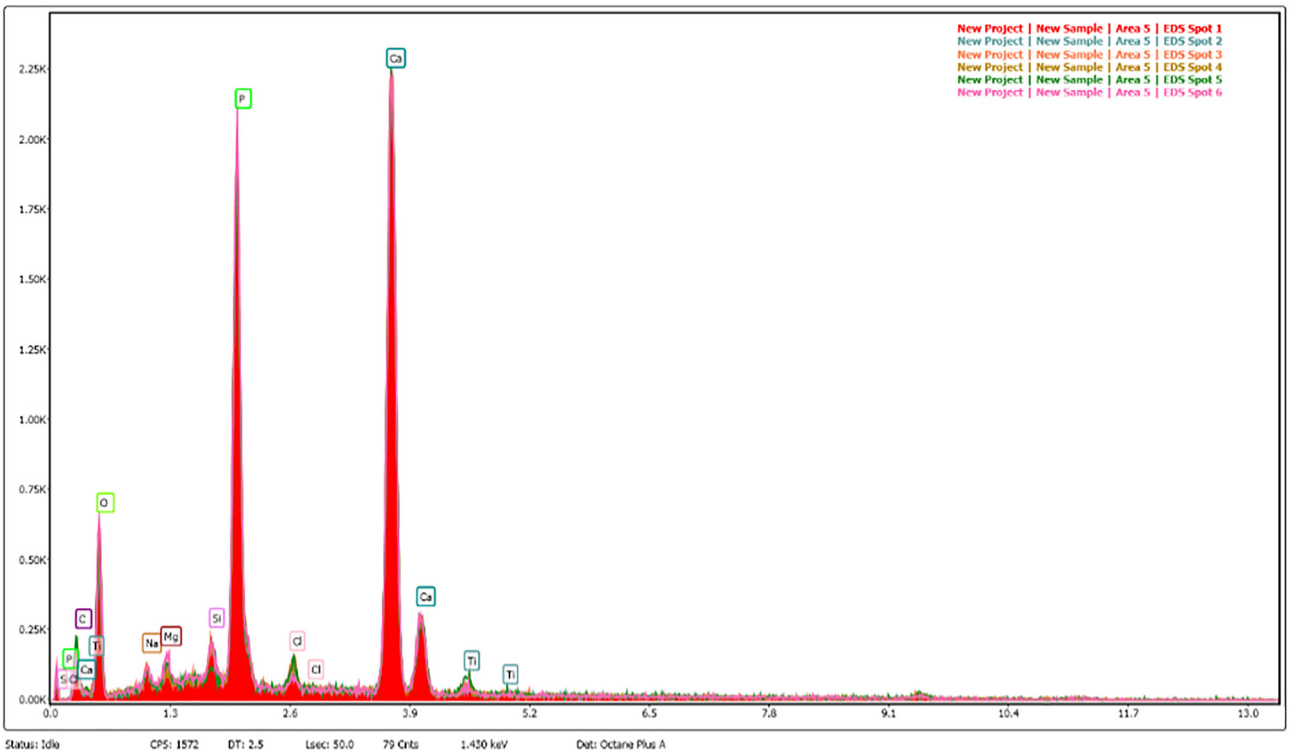

References

[1] A. Haleem, M. Javaid, R.H. Khan, R. Suman, 3D printing applications in bone tissue engineering, J. Clin. Orthopaed. Trauma 11 (2020) S118–S124.
[2] S.-Y. He, Y. Zhang, Y. Zhou, N. Bao, Y. Cai, P. Zhou, P. Wang, L. Li, Q. Jiang, Modeling osteoinduction in titanium bone scaffold with a representative channel structure, Mater. Sci. Eng., C 117 (2020) 111347.
[3] L.-C. Zhang, L.-Y. Chen, L. Wang, Surface modification of titanium and titanium alloys: technologies, developments, and future interests, Adv. Eng. Mater. 22 (2020) 1901258.
[4] Y. Dong, J. Tang, D. Wang, N. Wang, Z. He, J. Li, D. Zhao, M. Yan, Additive manufacturing of pure Ti with superior mechanical performance, low cost, and biocompatibility for potential replacement of Ti-6Al-4V, Mater. Des. 196 (2020) 109142.
[5] M. Kaur, K. Singh, Review on titanium and titanium based alloys as biomaterials for orthopaedic applications, Mater. Sci. Eng., C 102 (2019) 844–862.
[6] H. Qu, Additive manufacturing for bone tissue engineering scaffolds, Mater. Today Commun. 24 (2020) 101024.
[7] M.A. Ali, M. Rajabi, S. Sudhir Sali, Additive manufacturing potential for medical devices and technology, Curr. Opin. Chem. Eng. 28 (2020) 127–133.
[8] S. Rashia Begum, M. Saravana Kumar, C.I. Pruncu, M. Vasumathi, P. Harikrishnan, Optimization and fabrication of customized scaffold using additive manufacturing to match the property of human bone, J. Mater. Eng. Perform. 30 (7) (2021) 4848–4859.
[9] Y. Zhu, W.R. Wagner, Design principles in biomaterials and scaffolds, Principles Regenerat. Med. (2019) 505–522.
[10] H.-B. Kim, M. Hayashi, K. Nakatani, N. Kitamura, K. Sasaki, J.-I. Hotta, H. Masuhara, In situ measurements of ion-exchange processes in single polymer particles: laser trapping microspectroscopy and confocal fluorescence microspectroscopy, Anal. Chem. 68 (1996) 409–414.
[11] P. Dee, H.Y. You, S.-H. Teoh, H. Le Ferrand, Bioinspired approaches to toughen calcium phosphate-based ceramics for bone repair, J. Mech. Behav. Biomed. Mater. 112 (2020) 104078.
[12] A. Mumith, V.S. Cheong, P. Fromme, M.J. Coathup, G.W. Blunn, The effect of strontium and silicon substituted hydroxyapatite electrochemical coatings on bone ingrowth and osseointegration of selective laser sintered porous metal implants, PLoS One 15 (2020).
[13] S. Bose, D. Banerjee, A. Shivaram, S. Tarafder, A. Bandyopadhyay, Calcium phosphate coated 3D printed porous titanium with nanoscale surface modification for orthopedic and dental applications, Mater. Des. 151 (2018) 102–112.
[14] J.E. Biemond, G. Hannink, N. Verdonschot, P. Buma, Bone ingrowth potential of electron beam and selective laser melting produced trabecular-like implant surfaces with and without a biomimetic coating, J. Mater. Sci.-Mater. Med. 24 (3) (2013) 745–753.
[15] M.R. Casanova, C. Oliveira, E.M. Fernandes, R.L. Reis, T.H. Silva, A. Martins, N.M. Neves, Spatial immobilization of endogenous growth factors to control vascularization in bone tissue engineering, Biomater. Sci. 8 (9) (2020) 2577–2589.
[16] X. Lin, J. Chen, Y. Liao, J.L. Pathak, H. Li, Y. Liu, Biomimetic Calcium Phosphate Coating as a Drug Delivery Vehicle for Bone Tissue Engineering: A Mini-Review, Coatings 10 (11) (2020) 1118, https://doi.org/10.3390/coatings10111118.
[17] Y. Liu, E.B. Hunziker, P. Layrolle, J.D. De Bruijn, K. De Groot, Bone morphogenetic protein 2 incorporated into biomimetic coatings retains its biological activity, Tissue Eng. 10 (1-2) (2004) 101–108.
[18] L. Ding, Z.G. Sun, Z.L. Liang, F. Li, G.L. Xu, H. Chang, Investigation on Ti-6Al-4V microstructure evolution in selective laser melting, Metals 9 (2019) 1270.
[19] P. Ninpetch, P. Kowitwarangkul, S. Mahathanabodee, P. Chalermkarnnon, P. Rattanadecho, Computational investigation of thermal behavior and molten metal flow with moving laser heat source for selective laser melting process, Case Stud. Thermal Eng. 24 (2021) 100860.
[20] Y. Liu, K. Degroot, E. Hunziker, BMP-2 liberated from biomimetic implant coatings induces and sustains direct ossification in an ectopic rat model, Bone 36 (5) (2005) 745–757.
[21] Y. Liu, P. Layrolle, J. de Bruijn, C. van Blitterswijk, K. de Groot, Biomimetic coprecipitation of calcium phosphate and bovine serum albumin on titanium alloy, J. Biomed. Mater. Res. 57 (3) (2001) 327–335.
[22] E. Engvall, P. Perlmann, Enzyme-linked immunosorbent assay (ELISA) quantitative assay of immunoglobulin G, Immunochemistry 8 (9) (1971) 871–874.
[23] E. Astm, Standard test methods of compression testing of metallic materials at room temperature, ASTM International, West Conshohocken, PA, 2000, pp. 98–105.
[24] X. Lin, K. De Groot, D. Wang, Q. Hu, D. Wismeijer, Y. Liu, Suppl 1–M4: A review paper on biomimetic calcium phosphate coatings, Open Biomed. Eng. J. 9 (2015) 56.
[25] D. Halloran, H.W. Durbano, A. Nohe, Bone morphogenetic protein-2 in development and bone homeostasis, J. Develop. Biol. 8 (2020) 19.
[26] X. Zhang, X. Lin, T. Liu, L. Deng, Y. Huang, Y. Liu, Osteogenic enhancement between icariin and bone morphogenetic protein 2: A potential osteogenic compound for bone tissue engineering, Front. Pharmacol. 10 (2019) 201.
[27] G. Wu, Y. Liu, T. Iizuka, E.B. Hunziker, The effect of a slow mode of BMP-2 delivery on the inflammatory response provoked by bone-defect-filling polymeric scaffolds, Biomaterials 31 (29) (2010) 7485–7493.
[28] G. Wu, E.B. Hunziker, Y. Zheng, D. Wismeijer, Y. Liu, Functionalization of deproteinized bovine bone with a coating-incorporated depot of BMP-2 renders the material efficiently osteoinductive and suppresses foreign-body reactivity, Bone 49 (6) (2011) 1323–1330.
[29] G. Wu, Y. Liu, T. Iizuka, E.B. Hunziker, Biomimetic coating of organic polymers with a protein-functionalized layer of calcium phosphate: the surface properties of the carrier influence neither the coating characteristics nor the incorporation mechanism or release kinetics of the protein, Tissue Eng. Part C Methods 16 (2010) 1255–1265.
[30] T. Liu, G. Wu, D. Wismeijer, Z. Gu, Y. Liu, Deproteinized bovine bone functionalized with the slow delivery of BMP-2 for the repair of critical-sized bone defects in sheep, Bone 56 (1) (2013) 110–118.
[31] P. Jiang, J. Liang, R. Song, Y. Zhang, L. Ren, L. Zhang, P. Tang, C. Lin, Effect of octacalcium-phosphate-modified micro/nanostructured titania surfaces on osteoblast response, ACS Appl. Mater. Interfaces 7 (26) (2015) 14384–14396.
[32] F. Barrere, P. Layrolle, C. Van Blitterswijk, K. De Groot, Biomimetic calcium phosphate coatings on Ti6Al4V: a crystal growth study of octacalcium phosphate and inhibition by Mg2+ and HCO3−, Bone 25 (1999) 107S–111S.
[33] F. Barrere, P. Layrolle, C. Van Blitterswijk, K. De Groot, Biomimetic coatings on titanium: a crystal growth study of octacalcium phosphate, J. Mater. Sci. - Mater. Med. 12 (2001) 529–534.
[34] E.B. Hunziker, L. Enggist, A. Küffer, D. Buser, Y. Liu, Osseointegration: the slow delivery of BMP-2 enhances osteoinductivity, Bone 51 (2012) 98–106.
[35] Y. Liu, E.B. Hunziker, K. de Groot, P. Layrolle, Introduction of ectopic bone formation by BMP-2 incorporated biomimetically into calcium phosphate coatings of titanium-alloy implants, Key Eng. Mater. 240-242 (2003) 667–670.
[36] Y. Liu, C. Schouten, O. Boerman, G. Wu, J.A. Jansen, E.B. Hunziker, The kinetics and mechanism of bone morphogenetic protein 2 release from calcium phosphate-based implant-coatings, J. Biomed. Mater. Res. Part A 106 (9) (2018) 2363–2371.
[37] Y. Liu, E.B. Hunziker, N.X. Randall, K. de Groot, P. Layrolle, Proteins incorporated into biomimetically prepared calcium phosphate coatings modulate their mechanical strength and dissolution rate, Biomaterials 24 (1) (2003) 65–70.
[38] Y. Yan, H. Chen, H. Zhang, C. Guo, K. Yang, K. Chen, R. Cheng, N. Qian, N. Sandler, Y.S. Zhang, H. Shen, J. Qi, W. Cui, L. Deng, Vascularized 3D printed scaffolds for promoting bone regeneration, Biomaterials 190-191 (2019) 97–110.
[39] Y. Du, J.L. Guo, J. Wang, A.G. Mikos, S. Zhang, Hierarchically designed bone scaffolds: From internal cues to external stimuli, Biomaterials 218 (2019) 119334.
[40] L.J. Gibson, The mechanical behaviour of cancellous bone, J. Biomech. 18 (5) (1985) 317–328.
[41] G. Huang, S.-T. Pan, J.-X. Qiu, The osteogenic effects of porous Tantalum and Titanium alloy scaffolds with different unit cell structure, Colloids Surf., B 210 (2022) 112229, https://doi.org/10.1016/j.colsurfb.2021.112229.
[42] B. Eltlhawy, T. El-Midany, N. Fouda, I. Eldesouky, Finite Element Assessment of a Porous Tibial Implant Design Using Rhombic Dodecahedron Structure, Solid State Phenom. 318 (2021) 71–81.
[43] K.M. Abate, A. Nazir, Y.-P. Yeh, J.-E. Chen, J.-Y. Jeng, Design, optimization, and validation of mechanical properties of different cellular structures for biomedical application, Int. J. Adv. Manuf. Technol. 106 (3-4) (2020) 1253–1265.
[44] R. Wauthle, J. van der Stok, S. Amin Yavari, J. Van Humbeeck, J.-P. Kruth, A.A. Zadpoor, H. Weinans, M. Mulier, J. Schrooten, Additively manufactured porous tantalum implants, Acta Biomater. 14 (2015) 217–225.
[45] B. Zhang, X. Pei, C. Zhou, Y. Fan, Q. Jiang, A. Ronca, U. D'Amora, Y.u. Chen, H. Li, Y. Sun, X. Zhang, The biomimetic design and 3D printing of customized mechanical properties porous Ti6Al4V scaffold for load-bearing bone reconstruction, Mater. Des. 152 (2018) 30–39.
[46] M.A. Surmeneva, R.A. Surmenev, E.A. Chudinova, A. Koptioug, M.S. Tkachev, S. N. Gorodzha, L.-E. Rännar, Fabrication of multiple-layered gradient cellular metal scaffold via electron beam melting for segmental bone reconstruction, Mater. Des. 133 (2017) 195–204.
[47] G. Li, L. Wang, W. Pan, F. Yang, W. Jiang, X. Wu, X. Kong, K. Dai, Y. Hao, In vitro and in vivo study of additive manufactured porous Ti6Al4V scaffolds for repairing bone defects, Sci. Rep. 6 (2016) 34072.
[48] B. Vrancken, L. Thijs, J.-P. Kruth, J. Van Humbeeck, Heat treatment of Ti6Al4V produced by Selective Laser Melting: Microstructure and mechanical properties, J. Alloy. Compd. 541 (2012) 177–185.
[49] H.-C. Hsu, S.-K. Hsu, H.-K. Tsou, S.-C. Wu, T.-H. Lai, W.-F. Ho, Fabrication and characterization of porous Ti–7.5 Mo alloy scaffolds for biomedical applications, J. Mater. Sci. - Mater. Med. 24 (3) (2013) 645–657.
[50] H.-C. Hsu, S.-C. Wu, S.-K. Hsu, T.-Y. Chang, W.-F. Ho, Effect of ball milling on properties of porous Ti–7.5 Mo alloy for biomedical applications, J. Alloy. Compd. 582 (2014) 793–801.
[51] H.-C. Hsu, S.-C. Wu, S.-K. Hsu, M.-S. Tsai, T.-Y. Chang, W.-F. Ho, Processing and mechanical properties of porous Ti–7.5 Mo alloy, Mater. Des. 47 (2013) 21–26.
[52] M. Monzón, C. Liu, S. Ajami, M. Oliveira, R. Donate, V. Ribeiro, R.L. Reis, Functionally graded additive manufacturing to achieve functionality specifications of osteochondral scaffolds, Bio-Design Manuf. 1 (1) (2018) 69–75.

[53] E. Onal, J.E. Frith, M. Jurg, X. Wu, A. Molotnikov, Mechanical properties and in vitro behavior of additively manufactured and functionally graded Ti6Al4V porous scaffolds, Metals 8 (2018) 200.
[54] S. Wang, L.L. Liu, K. Li, L.C. Zhu, J. Chen, Y.Q. Hao, Pore functionally graded Ti6Al4V scaffolds for bone tissue engineering application, Mater. Des. 168 (2019) 107643.
[55] D. Khrapov, A. Koptyug, K. Manabaev, F. Léonard, T. Mishurova, G. Bruno, D. Cheneler, K. Loza, M. Epple, R. Surmenev, M. Surmeneva, The impact of post manufacturing treatment of functionally graded Ti6Al4V scaffolds on their surface morphology and mechanical strength, J. Mater. Res. Technol. 9 (2) (2020) 1866–1881.
[56] J.M. Lowen, J.K. Leach, Functionally graded biomaterials for use as model systems and replacement tissues, Adv. Funct. Mater. 30 (2020) 1909089.
[57] R. Guillot, F. Gilde, P. Becquart, F. Sailhan, A. Lapeyrere, D. Logeart-Avramoglou, C. Picart, The stability of BMP loaded polyelectrolyte multilayer coatings on titanium, Biomaterials 34 (23) (2013) 5737–5746.
[58] D. Ražem, B. Katušin-Ražem, The effects of irradiation on controlled drug delivery/controlled drug release systems, Radiat. Phys. Chem. 77 (3) (2008) 288–344.
[59] U. Ripamonti, B. Van den heever, J. Crooks, M.M. Tucker, T.K. Sampath, D.C. Rueger, A.H. Reddi, Long-term evaluation of bone formation by osteogenic protein 1 in the baboon and relative efficacy of bone-derived bone morphogenetic proteins delivered by irradiated xenogeneic collagenous matrices, J. Bone Miner. Res. 15 (9) (2000) 1798–1809.
[60] S. Wientroub, A.H. Reddi, Influence of irradiation on the osteoinductive potential of demineralized bone matrix, Calcif. Tissue Int. 42 (4) (1988) 255–260.
[61] T. Pekkarinen, T. Jämsä, M. Määttä, O. Hietala, P. Jalovaara, Reindeer BMP extract in the healing of critical-size bone defects in the radius of the rabbit, Acta orthopaedica 77 (6) (2006) 952–959.